-Electronic Supporting Information -

Alcohol Oxidation with High Efficiency and Selectivity by Nickel Phosphide Phases

Sirshendu Ghosh,[a] Biswajit Mondal,[a] Shubasis Roy,[a] Menny Shalom*[a] and Maya Bar Sadan*[a]

[a]*Department of Chemistry, Ben Gurion University, Beer-Sheva, 8410501 Israel.*

*barsadan@bgu.ac.il *mennysh@bgu.ac.il

Materials:

Nickel acetylacetonate (Ni(acac)$_2$, 99.9%, Acros organics), Oleylamine (OLAM, 70%, tech), octadecene (ODE), trioctylphosphine (TOP, 97%), hexafluorophosphoric acid (HPF$_6$, 65 wt%), Nickel nitrate hexahydrate (Ni(NO$_3$)$_2$.6H$_2$O), potassium persulfate ($K_2S_2O_8$), Formamide were purchased from Sigma-Aldrich. All chemicals were used as received without any purification. Ethylene Glycol, Glycerol were purchased from Merck chemicals. Solvents used for storage, washing and catalysis were purchased from Gadot and Romical. Water used for cleaning the electrode and electrochemical measurement was with resistance 18.2 MΩ cm.

Ni_2P and $Ni_{12}P_5$ synthesis: 2.5 mmol nickel acetylacetonate (Ni(acac)$_2$), 7.5 ml octadecene (ODE), 5 ml oleylamine (OLAM), and trioctylphosphine (TOP) (0.75 ml for $Ni_{12}P_5$ synthesis or 1.8 ml for Ni_2P synthesis) were mixed together in a round-bottom flask and heated to 100 °C for 30 min in vacuum. The flask was backfilled with dry nitrogen and heated to 300 °C at a heating rate of 10 °C/min. The temperature was maintained for 45 min before the flask was allowed to cool down to ambient temperature. The products were collected by centrifugation using chloroform as a solvent and ethanol as a non-solvent.

Ni_5P_4 synthesis: 1 mmol Ni(acac)$_2$, 4 ml OLAM, and 2 ml ODE were mixed and heated to 120 °C for 30 min in a round-bottom flask with continuous evacuation. In another round-bottom flask, 3 ml TOP was degassed and heated to 350 °C, after which the Ni–OLAM solution was injected. The reaction lasted 20 min at 350 °C before it was let to cool down to ambient temperature. The washing process was the same as for the other synthesis.

Synthesis of $Ni(OH)_2$ and NiOOH:

First, 100 mg Ni(NO$_3$)$_2$. 6 H$_2$O was dissolved in 10 ml DI H$_2$O and heated to 60 ^{0}C, then 5 ml 0.5 M NaOH solution was added dropwise with continuous stirring for 1 hr. The green color product was collected by centrifugation. The washing process was carried out for two times with DI H$_2$O and one time with acetone. The product was dried in at 80 °C in a vacuum oven.

For the synthesis of NiOOH, the as-synthesized Ni(OH)$_2$ was dispersed in 15 ml 6 M KOH heated at 60 °C. Excess of $K_2S_2O_8$, 5 ml 32% H_2O_2 were added and kept at 60 °C for 16 hr. The black color product was collected by centrifugation. The washing process was repeated for three times with DI water and once with acetone. The product was dried overnight under vacuum at 100 °C.

Electrocatalytic measurements for OER and alcohol oxidation:

The surface capping OLAM and TOP ligands were exchanged with PF^{6-} anions (HPF_6 in formamide) to make the nanoparticles water dispersible and to expose the catalytic sites. For the electrochemical experiments, catalyst ink was prepared by mixing 1 mg of the ligand-stripped nanocrystals, 1 mg carbon black, and 410 µL Nafion solution (from a mixture of 200 µL DI H_2O, 200 µL isopropanol, and 10 µL 5% Nafion solution). All the materials were blended and sonicated for 30 min to form the catalyst ink. The glassy carbon electrodes (3 mm in diameter) were cleaned with alumina micro-polishing powder (0.05 µm) followed by ultrasonication in ethanol and water for 30 s. The homogeneous ink (20 µL) was drop-casted onto a mirror-polished 3-mm glassy carbon electrode to form a final loading of ~0.7 mg cm^{-2} (0.049 mg/0.0706 cm^{-2} = 0.693 mg cm^{-2}) and was left overnight to dry under ambient conditions. The electrochemical OER and alcohol oxidation reactions measurements were performed in 1.0 M NaOH aqueous solution at room temperature using Ag/AgCl (with saturated KCl) reference electrode.

Polarization curves were recorded on an Ivium Technologies Vertex potentiostat/galvanostat(V74606) and analyzed using the IviumSoft program. All measurements were referred to the RHE using the relationship: $E(RHE) = E(Ag/AgCl) + E_0(Ag/AgCl) + 0.059V \times pH$.

Electrochemical impedance spectroscopy (EIS) measurements were carried out at various potentials within the frequency range 100 kHz–0.05 Hz with an amplitude of 15 mV. R_{ct} values were determined by fitting the obtained semicircle with R (RC) circuit.

Electrochemical active surface area (ECSA) was derived from double layer capacitance (C_{dl}) value using the following formulae:

$$ECSA = \frac{C_{dl}}{0.04}$$

The activation energy was derived by performing chrono amperometry study at four different temperatures at four different potentials (kinetic region of catalysis). Temperature was maintained by a temperature controller with thermocouple. The activation energy was derived from log*I* *vs* 1/T plot.

Before the alcohol oxidation reaction (Data presented in Fig. 2 and 4), each electrode was activated by running 5 CV cycles in 0 V to 0.5 V (vs Ag/AgCl) range in 1 M NaOH.

Materials Characterizations

XRD: Panalytical Empyrean powder X-ray diffractometer equipped with a position sensitive X'Celerator detector using Cu Kα radiation (λ = 1.5405 Å) operated at 40 kV and 30 mA.

TEM: High resolution transmission electron microscopy (HRTEM) imaging was carried out using a JEOL JEM-2100F analytical TEM operating at 200 keV equipped with GATAN 894 US1000 camera. Energy-Dispersive X-ray Spectroscopy (EDS) analysis was performed using a JEOL JEM-2100F TEM operating at 200 kV equipped with a JED-2300T energy dispersive X-ray spectrometer. Scanning TEM (STEM) images were taken using an GATAN 806 HAADF STEM detector. The probe size during the analysis was set to 2 nm. JEOL Analytical Station software (v. 3.8.0.21) was used for the EDS data analysis. The quantitative analysis was performed by the standard less Cliff–Lorimer method.

XPS: X-ray photoelectron spectrometer ESCALAB 250 ultrahigh vacuum (1×10^{-9} bar) apparatus with an Al Kα X-ray source and a monochromator.

FTIR: Infrared (FTIR) spectra were acquired from KBr pellets using a Nicolet Impact 410 spectrophotometer.

NMR: NMR spectra were acquired on a Bruker 400 MHz instrument.

Ligand stripping

Procedure: To make the nanocrystals surface more catalytically active, we replaced the long organic chained OLAM and TOP with PF_6^- ligand. Dried powder of the as-synthesized nanocrystals (10 mg) was dissolved in 2 ml $CHCl_3$ and mixed with equal volume of HPF_6 solution (in formamide). The mixture was agitated in a vortex genie for 2 min. Within 1 min, the ligand exchanged nanocrystals were flocculated. The mixture was centrifuged at 6000 rpm for 5 min and the product re-dissolved in 1 ml $CHCl_3$ and the same volume of HPF_6 solution. The solution was agitated for 2 min for complete removal of the organic ligands and centrifuged. The product was re-dissolved in 2 ml of $CHCl_3$ and 2 ml of acetone and sonicated mildly for 3 min, and then the nanocrystals were collected by centrifugation. The washing process was repeated two times for a complete removal of OLAM, TOP and unreacted HPF6. The collected product was vacuum-dried and stored in a glovebox.

Fig. S1 shows the FTIR spectra of OLAM, TOP and as-synthesized $Ni_{12}P_5$. For the as-synthesized $Ni_{12}P_5$ sample, the stretching vibration of the -C-H- group of OLAM at 2854.5 cm^{-1} and TOP at 2921.28 cm^{-1} and the bending vibration of -C-N- and –N-H- of OLAM at 1060 cm^{-1} and 1555 cm^{-1} were identified in the spectrum. This observation along with the shifting and broadening of the bands confirmed the binding of OLAM onto the nanocrystals' surface. The absence of the stretching modes of -C-N-, –N-H- and –C=C- after the ligand exchange confirmed the complete elimination of OLAM and TOP from the nanocrystals' surface.

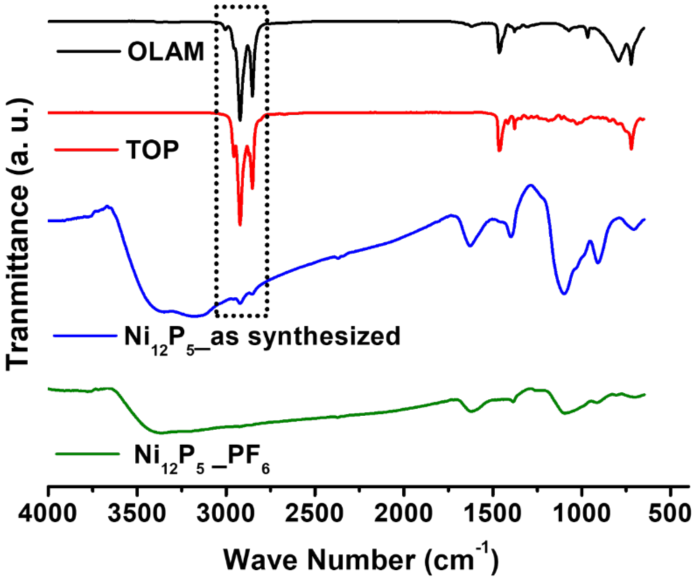

Fig. S1 FTIR spectra of as-synthesized nanoparticles, OLAM, TOP and the nanoparticles after ligand exchange to PF_6.

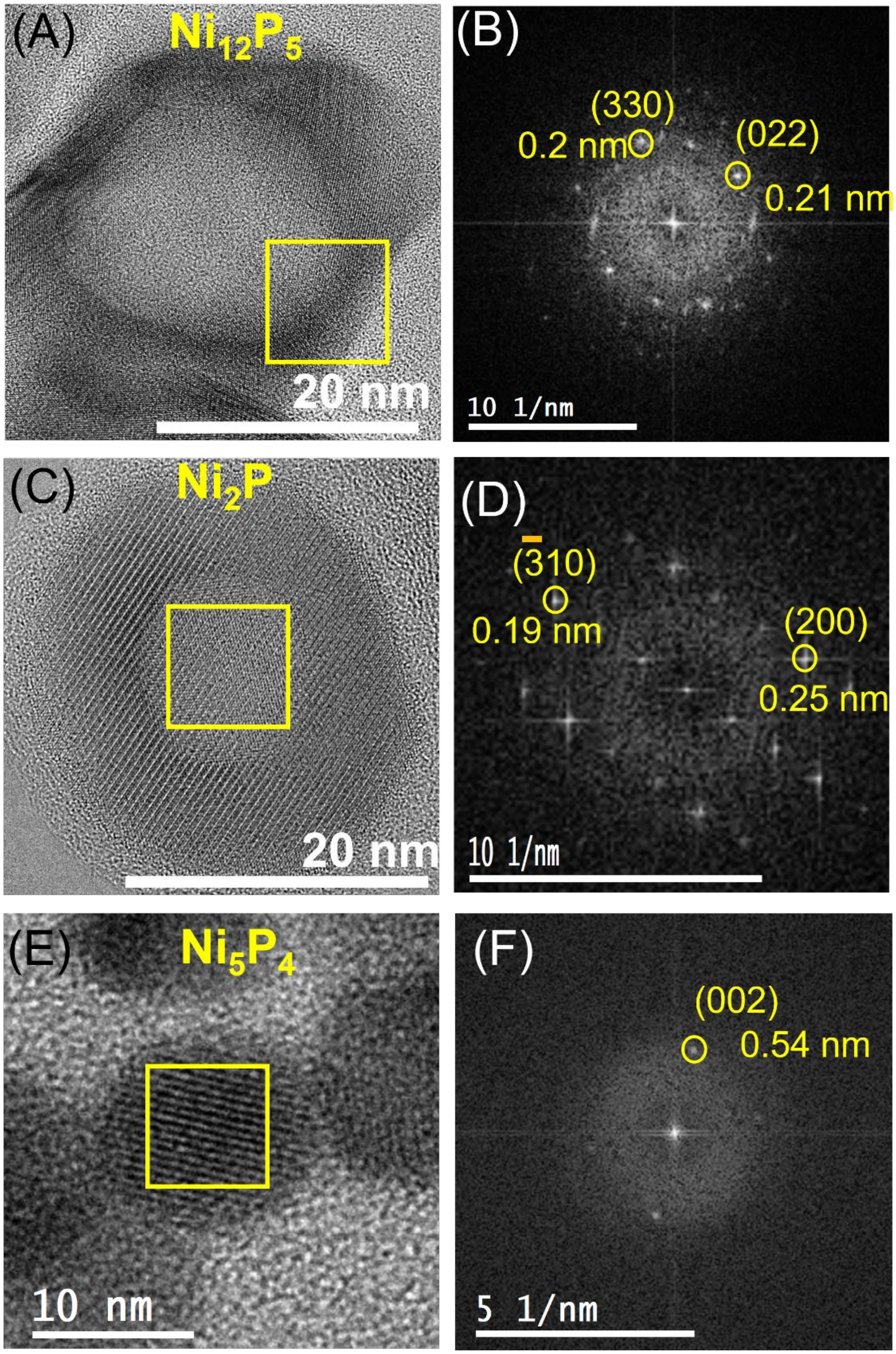

Fig. S2 HRTEM images of (A) $Ni_{12}P_5$, (B) Ni_2P and (C) Ni_5P_4 showing that the particle comprises a single domain.

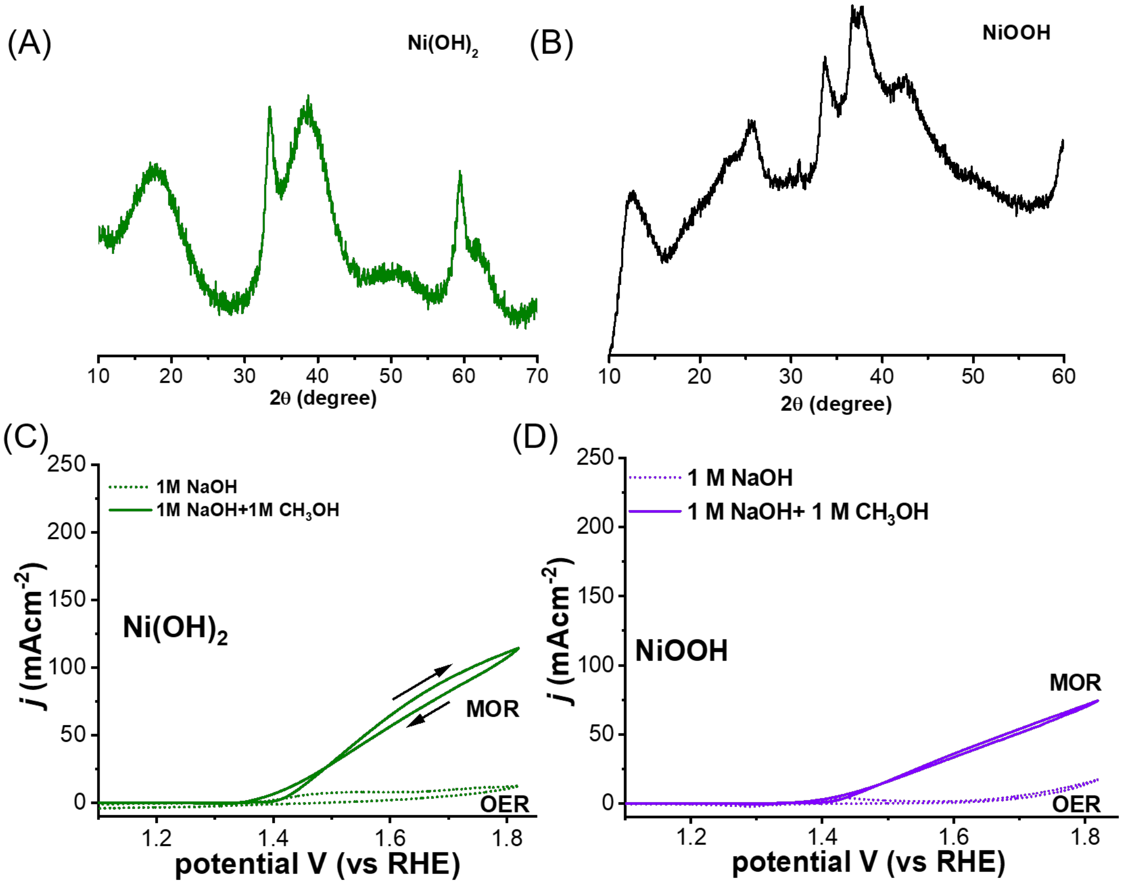

Fig. S3 XRD patterns of the reference samples and their catalytic activity. (A,C) β-Ni(OH)$_2$ (JCPDS No: 14-0117) and (B,D) NiOOH (JCPDS card NO: 06-0075).

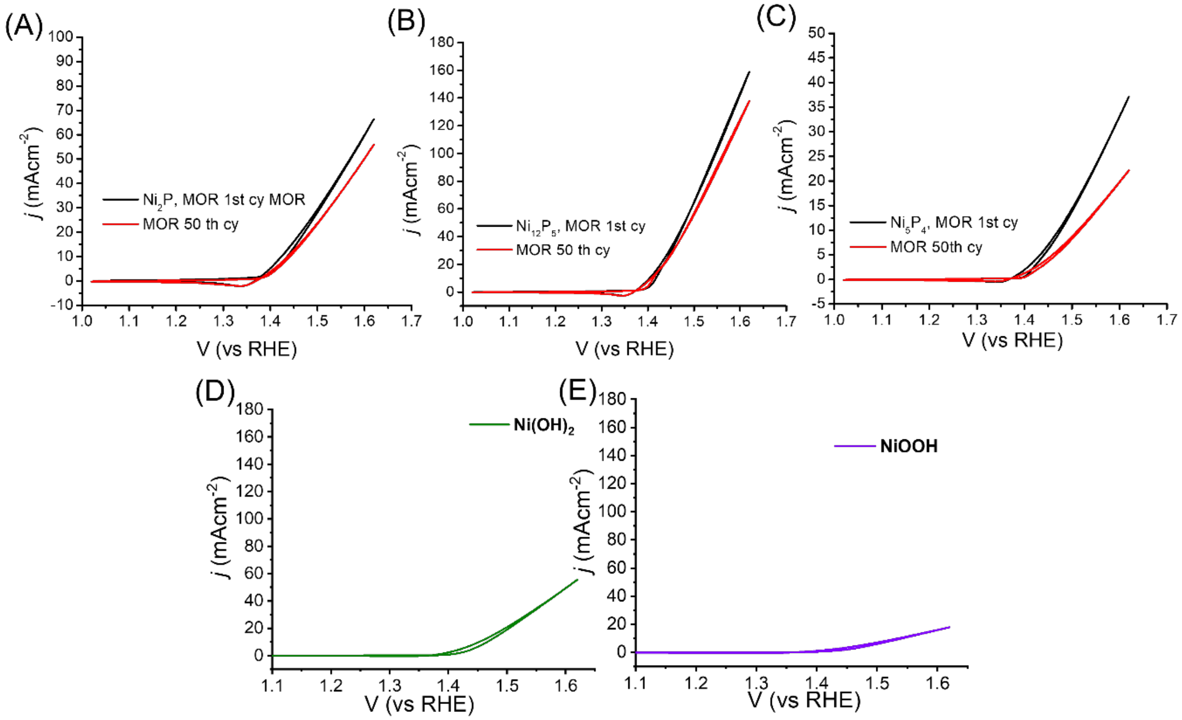

Fig. S4 Current densities of (A-C) $Ni_{12}P_5$, Ni_2P, Ni_5P_4 catalyst at first and 50th cycles of MOR CV. (D) $Ni(OH)_2$ and (E) NiOOH after 50 cycles of MOR (1 M NaOH + 1 M CH_3OH).

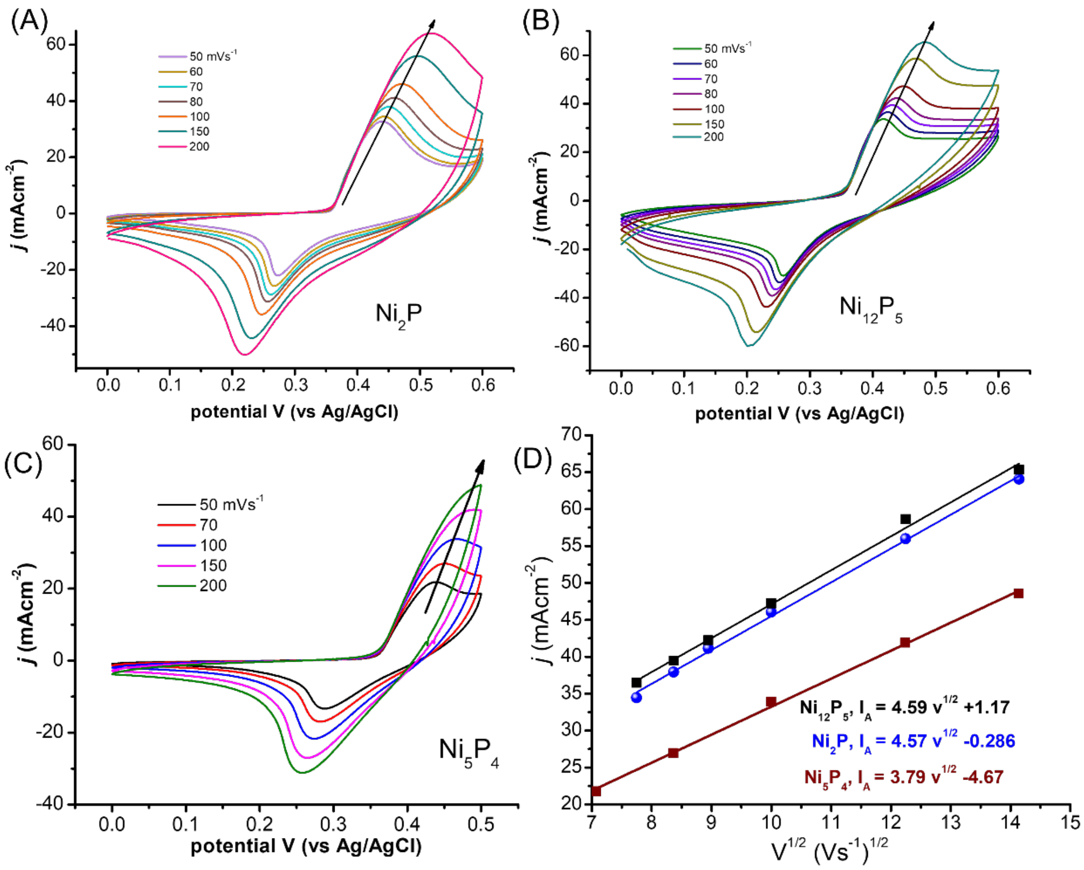

Fig. S5 CVs in the Ni^{2+}/Ni^{3+} redox couple region at different scan rates of (A) Ni_2P, (B) $Ni_{12}P_5$ and (C) Ni_5P_4 (D) Linear fitting of the peak current densities as a function of the square root of the scan rate (50 to 150 mVS^{-1}).

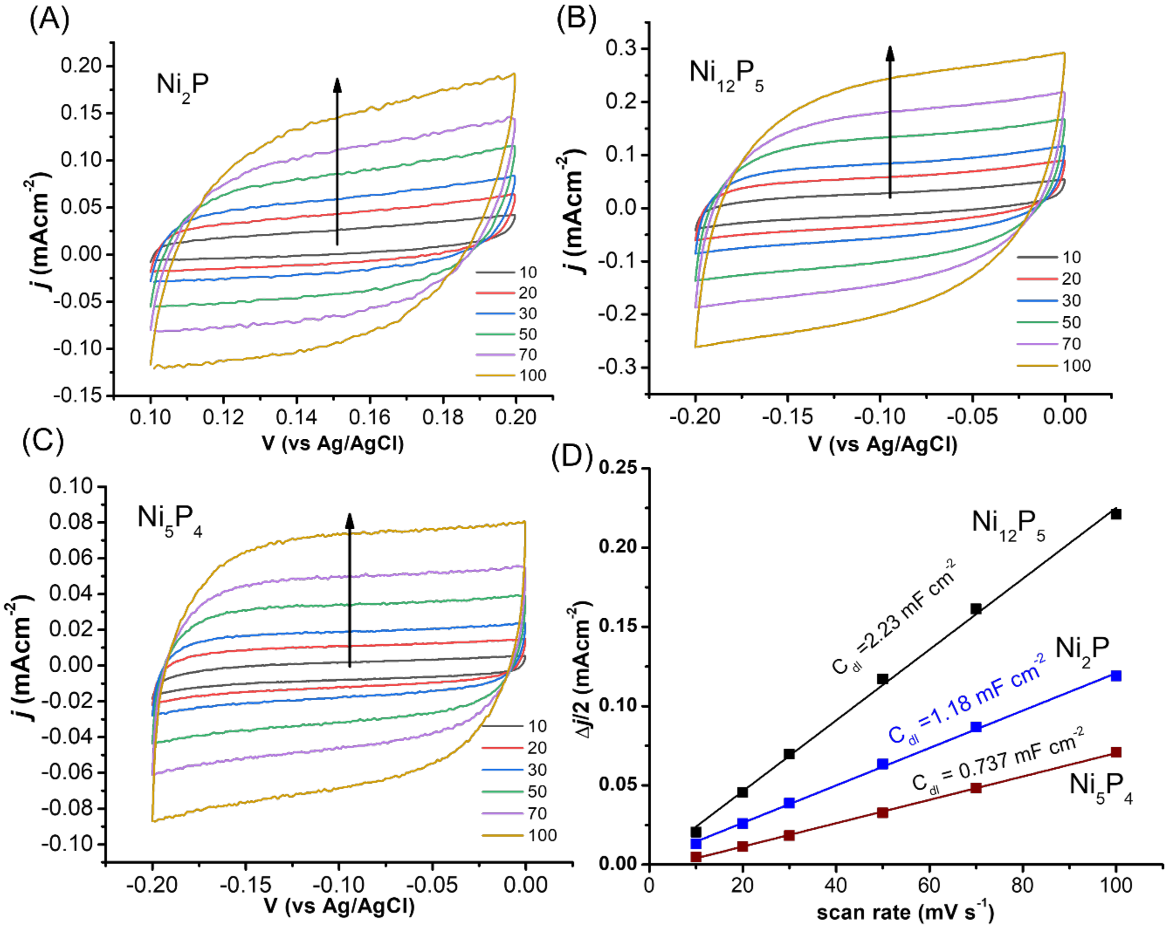

Fig. S6 (A-C) Initial CVs of Ni_2P, $Ni_{12}P_5$ and Ni_5P_4 at different scan rates in the non-Faradic region. (D) Comparative double layer capacitance plots.

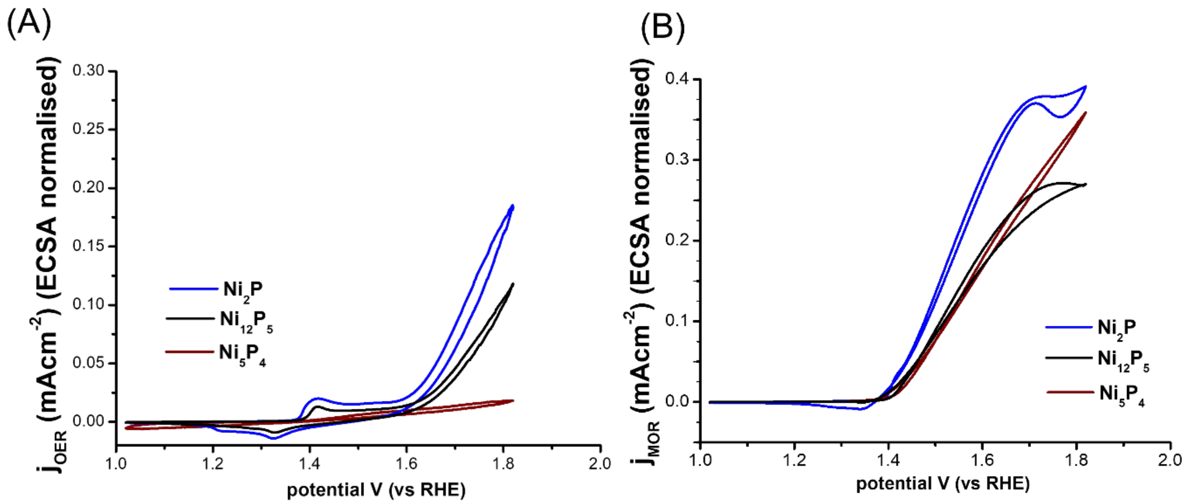

Fig. S7 (A-B) ECSA normalized OER and MOR LSV plots for all the catalysts.

The activation energy was determined from the Arrhenius plot of log I vs 1/T at the kinetic region of catalysis. The increased I value with temperature is attributed to the increased adsorption and diffusion of OH^- ions from the solution which resulted in higher population of the active species for catalysis. **Fig. 3E** shows the comparative activation energy plots for the two catalysts at different potentials, derived from slopes in **Fig. S8 (C)** and **(D)**.

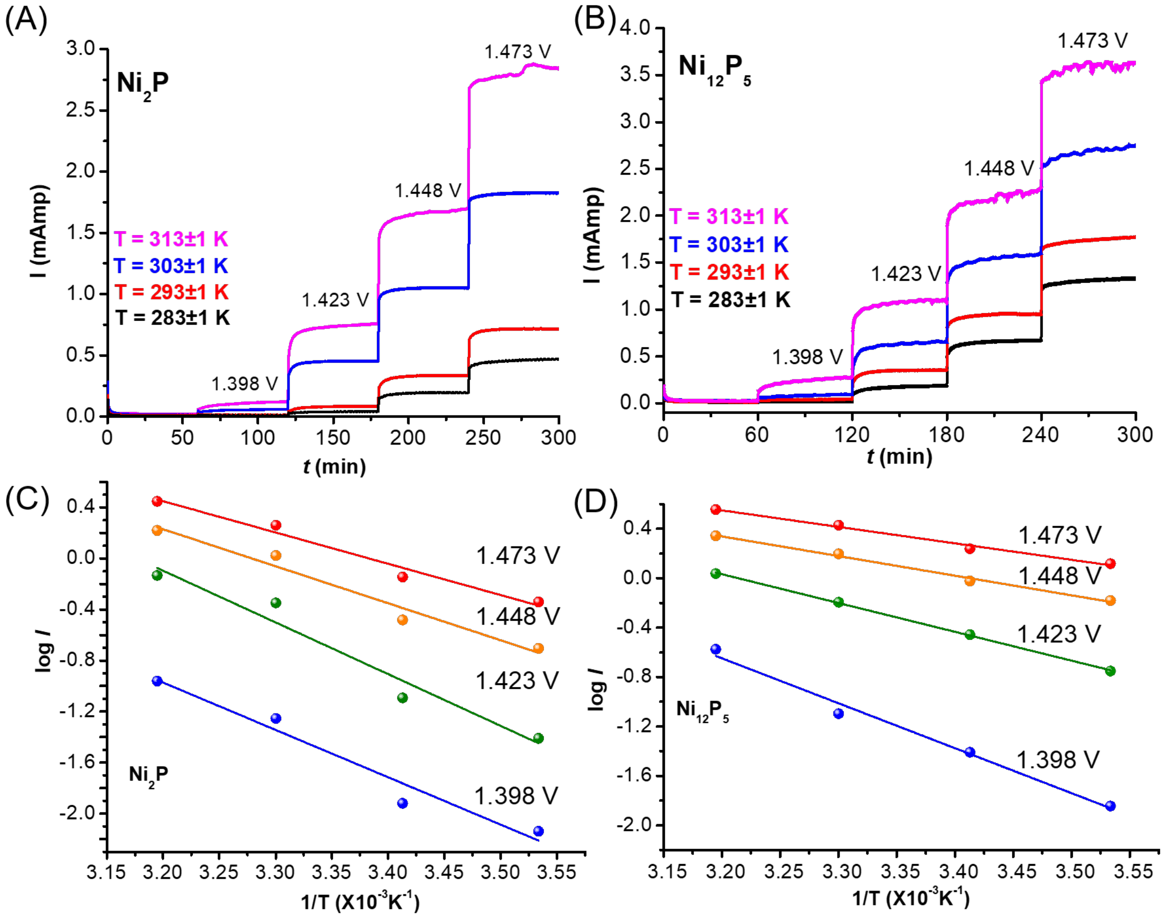

Fig. S8 Chrono-amperometry plot of (A) Ni_2P and (B) $Ni_{12}P_5$, in 1M NaOH+1 M CH_3OH at different potentials vs RHE at four different temperatures. The corresponding Arrhenius plots at different potentials for (C) Ni_2P and (D) $Ni_{12}P_5$.

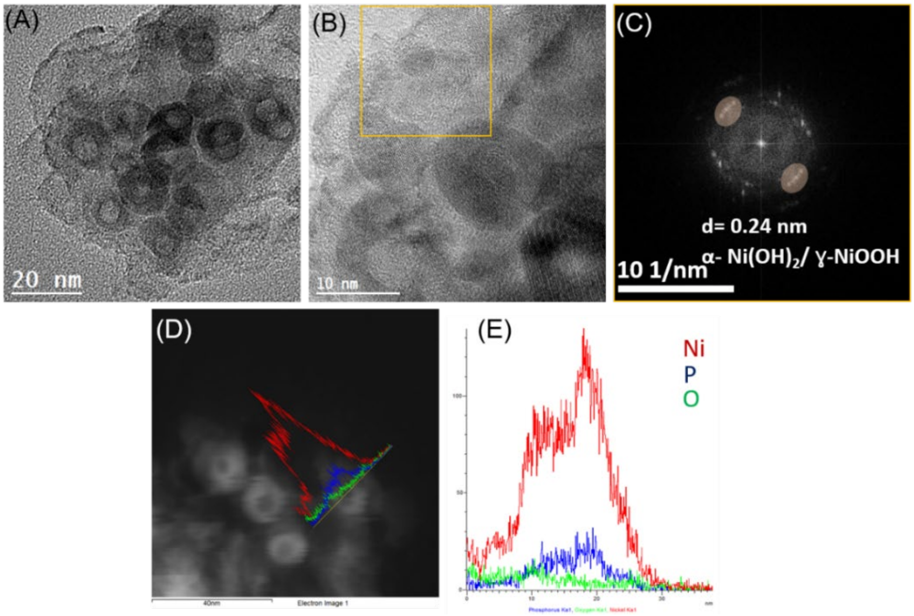

Fig. S9 Microscopy images of $Ni_{12}P_5$ after 50 **OER** cycles. (A) TEM. (B-C) HRTEM and FFT shows the presence of polycrystalline $Ni(OH)_2$/NiOOH species on the surface. (D-E) STEM and a EDS line scan showing the presence of nickel and oxygen on the surface of the $Ni_{12}P_5$, but almost no P.

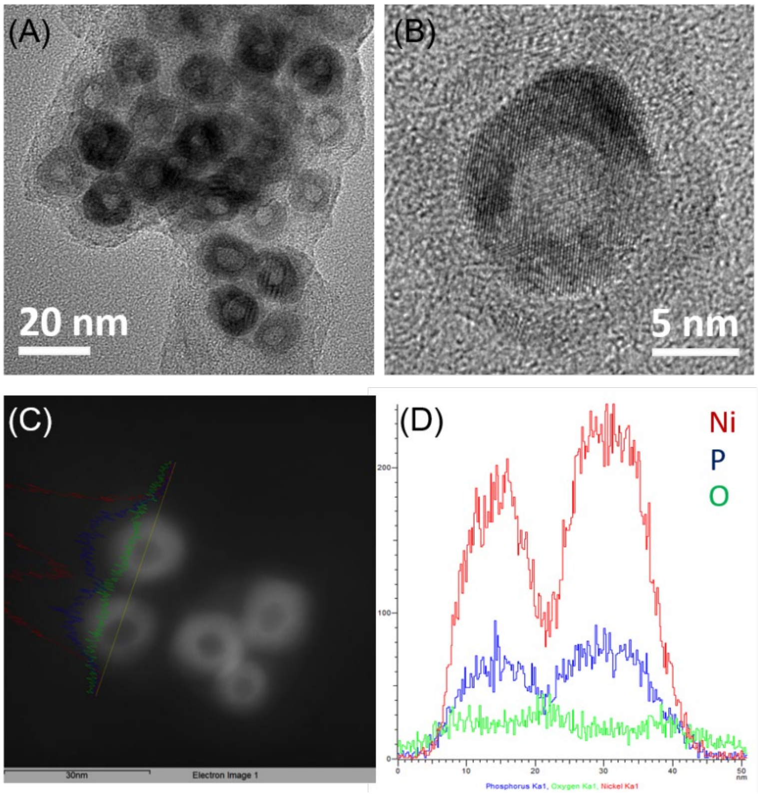

Fig. S10 Microscopy images of $Ni_{12}P_5$ after 50 **MOR** cycles. (A) TEM. (B) HRTEM. (C-D) STEM and EDS line scan showing the existence of P until the surface of the structure, with minimal oxidized nickel layer.

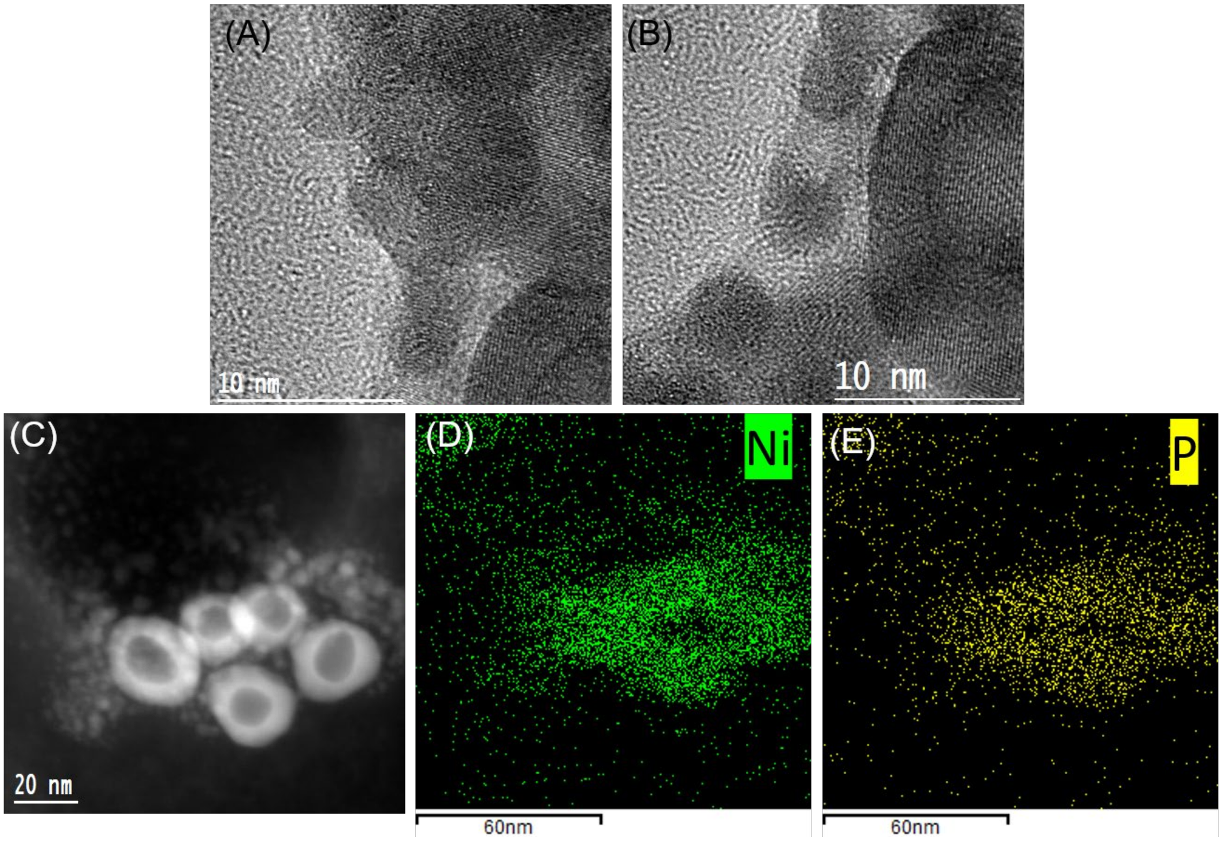

Fig. S11 Microscopy images of Ni_2P after 50 **OER** cycles. (A-B) HRTEM. (C) STEM and (D-E) element mapping showing the overlapping of P and Ni.

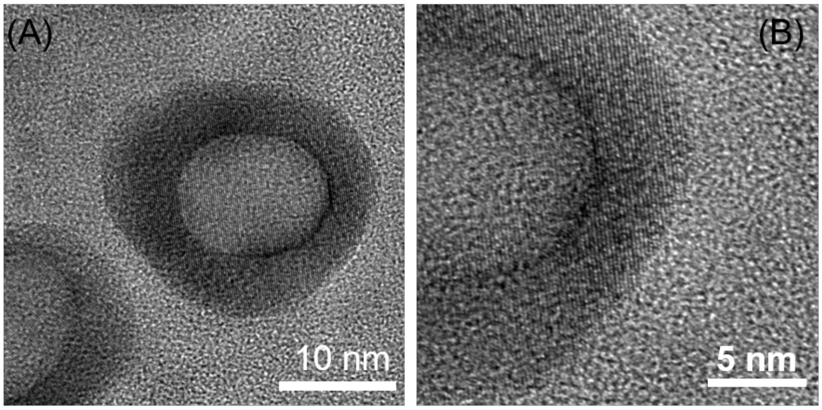

Fig. S12 Microscopy images of Ni_2P after 50 **MOR** cycles showing the absence of $Ni(OH)_2$/NiOOH species on the surface.

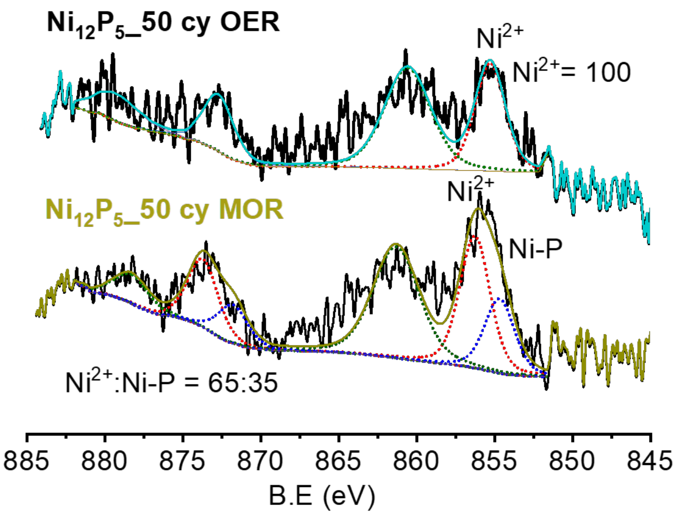

Fig. S13 XPS spectra of the Ni signal in Ni$_{12}$P$_5$ after 50 cycles of OER or MOR.

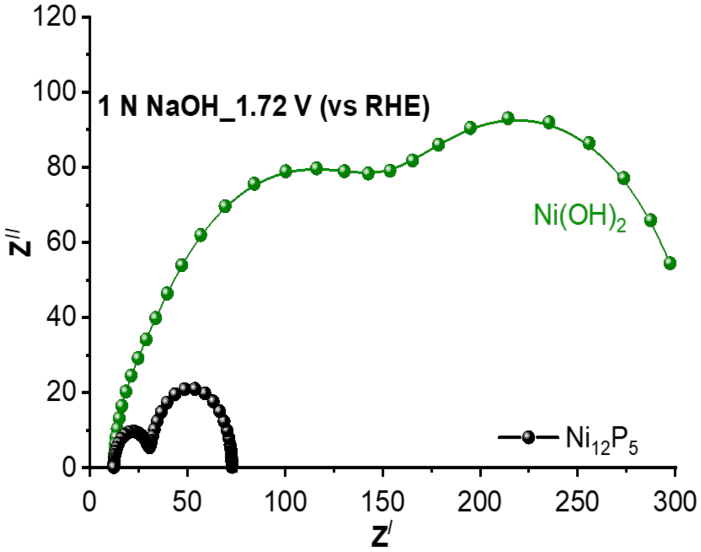

Fig. S14 Nyquist plots of Ni$_{12}$P$_5$ and Ni(OH)$_2$ in 1 M NaOH at a bias of 1.72 V vs RHE.

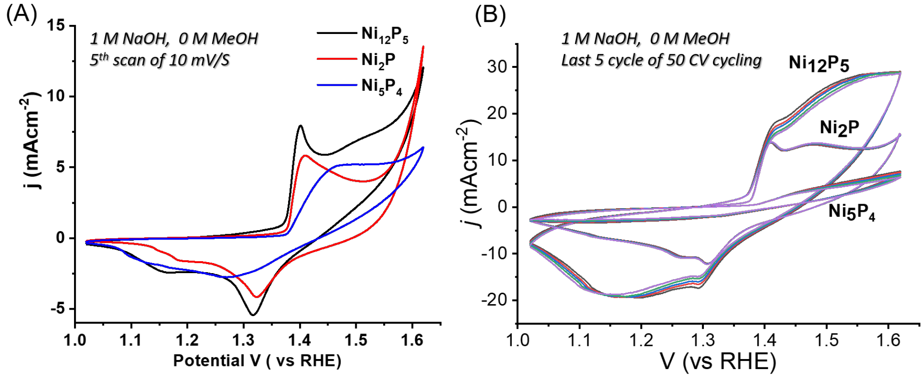

Fig. S15 CV of the various nickel phosphide phases in 1 M NaOH in the range of 0.0 to 0.6 V (vs Ag/AgCl) at a scan rate of 10 mVs^{-1} (A) After the 5th OER cycle. (B) Cycles 46-50. The current density of different catalysts follows the trend seen in the study: $Ni_{12}P_5$ > Ni_2P > Ni_5P_4.

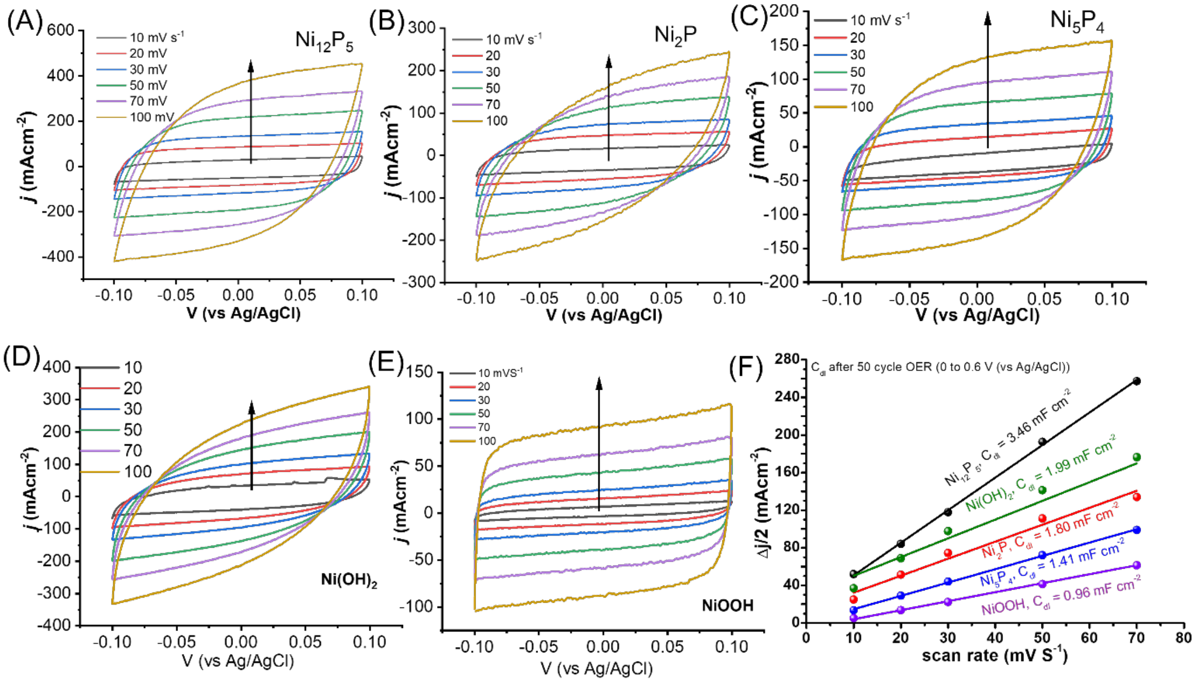

Fig. S16 CV curves after 50 cycles of OER at different scan rates in a non-Faradaic region: (A-E) $Ni_{12}P_5$, Ni_2P, Ni_5P_4, $Ni(OH)_2$ and NiOOH respectively. (F) The corresponding linear fitting of the difference between the anodic and cathodic currents (*ΔJ*) versus scan rate to estimate the double layer capacitance (C_{dl}).

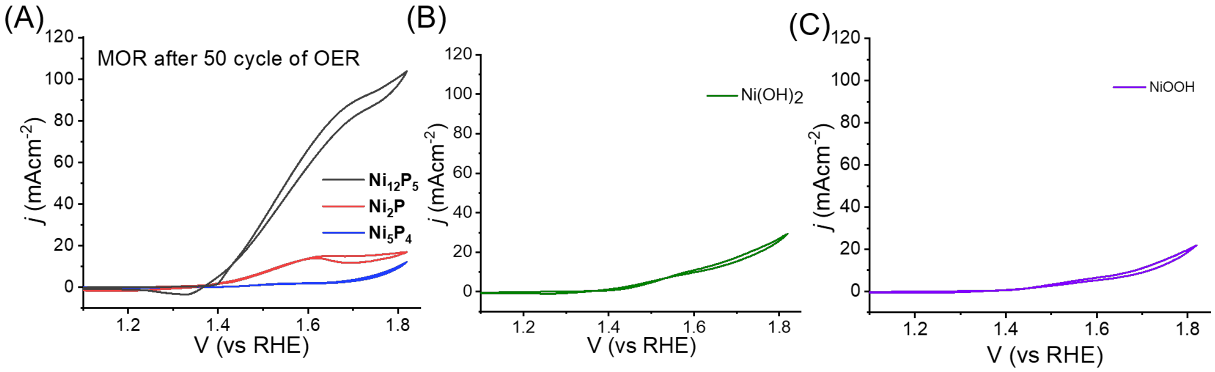

Fig. S17 CVs for samples that were subjected to 50 cycles of OER in 1 M NaOH and then measured for MOR.

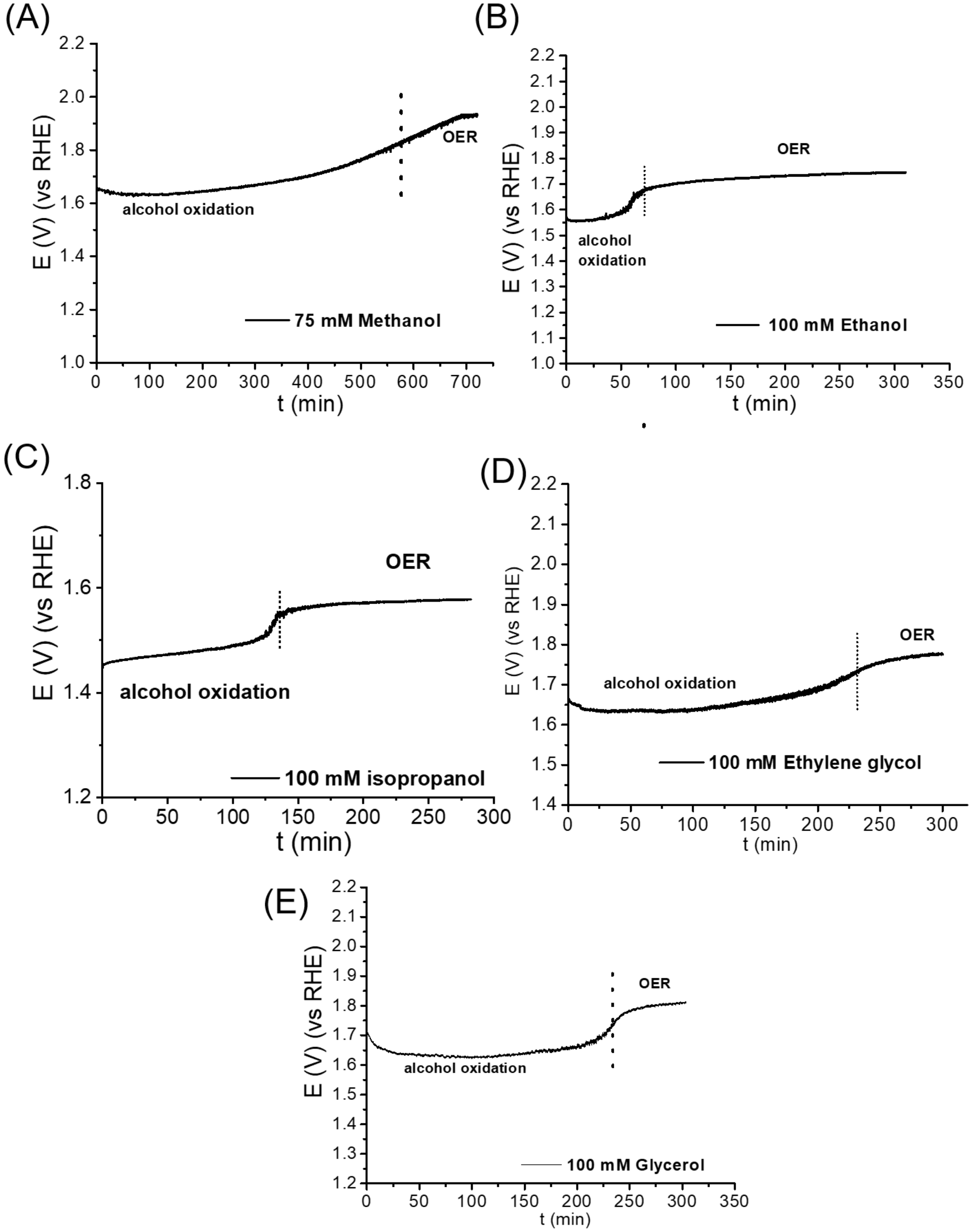

Fig. S18 Chronopotentiometry for alcohol oxidations in 1M NaOH at a current density of 50 mAcm^{-2}. The catalyst loading was 1 mg over 1 cm^2 of carbon cloth and the total volume of the electrolyte was 10 mL. Each of *E*-t plots shows two distinct regions: first only alcohol oxidation and later, once the alcohol was consumed, OER became dominant.

Table S1. Comparative Table of performances of different catalysts for different alcohol oxidation reaction in alkaline medium.*

Electrocatalyst	*Electrolyte solution*	*Catalytic performances*			*Reference*
		Potential (V) (vs RHE)	*mA cm^{-2}*	*A mg^{-1}*	
Methanol oxidation					
$Ni_{12}P_5$ nanoparticles	**1.0 M KOH + 1.0 M methanol**	**1.72**	**210**	**4.236**	**This Work**
Ni_2P nanoparticles	**1.0 M KOH + 1.0 M methanol**	**1.72**	**112.6**	**2.23**	**This work**
Branched Ni_3C particles/C	1.0 M KOH + 1.0 M methanol	1.64	126.7	4.2	[1]
NiO@C/CC	1.0 M KOH + 1.0 M methanol	1.82	188.6	3.14	[2]
(110)-facet rich Ni nanocrystal	1.0 M KOH + 1.0 M methanol	1.55	61	2.02	[3]
FeNi NPs	1.0 M KOH + 1.0 M methanol	1.7	-	1.71	[4]
$Ni_{1.7}Sn$ NPs/CB	0.5 M KOH + 0.5 M methanol	1.57	50.9	0.82	[5]
Urchin-like Ni-Co-P-O	0.5 M KOH + 1.0 M methanol	1.65		1.57	[6]
3D Ni-P-O	0.5 M KOH + 1.0 M methanol	1.42		1.48	[7]
Ni-P NWs/rGO	1.0 M NaOH + 0.5 M methanol	1.55	16.4	0.12	[8]
Mesoporous NiP	0.1 M NaOH + 1.0 M methanol	1.51	1.7		[9]
Branched $Ni_{0.75}Cu_{0.25}$ Networks	1.0 M NaOH + 0.5 M methanol	1.74	84	0.17	[10]
NiO layer/CNTs	1.0 M KOH + 0.5 M methanol	1.68	131.4		[11]
NiSe Nanowire	1.0 M KOH + 0.5 M methanol	1.47	132		[12]
$NiCo_2O_4$/MWCNTs	1.0 M KOH + 1.0 M methanol	1.67	153.5	0.11	[13]
Ethanol oxidation					
$Ni_{12}P_5$ nanoparticles	**1.0 M KOH + 1.0 M Ethanol**	**1.65**	**175**	**3.54**	**This work**
Ni_2P nanoparticles	**1.0 M KOH + 1.0 M Ethanol**	**1.65**	**138**	**2.8**	**This work**
NiO@C/CC	1.0 M KOH + 1.0 M ethanol	1.82	119.1	1.985	[2]
LDH@MnO_2	1.0 M KOH + 1.0 M ethanol	1.67	4.5	-	[14]
Ni-NPs	1.0 M KOH + 1.0 M ethanol	1.823	47	-	[15]

Ni$_x$Co$_{1-x}$ alloy	1.0 M KOH + 5.0 M ethanol	1.88	142	-	*16*
NiNC-4	0.1 M KOH + 1.0 M ethanol	1.69	327	-	17
Ethylene glycol oxidation					
Ni$_{12}$P$_5$ nanoparticles	**1.0 M KOH + 1.0 M ethylene glycol**	**1.65**	**94**	**1.91**	**This Work**
Ni$_2$P nanoparticles	**1.0 M KOH + 1.0 M ethylene glycol**	**1.65**	**45**	**0.911**	**This Work**
PdFePb Nanowire	0.5 M KOH + 0.5 M ethylene glycol	0.96	105	3.19 (per mg$_{Pd}$)	18
Pd/C	0.5 M KOH + 0.5 M ethylene glycol	0.96	-	0.57 (per mg$_{Pd}$)	18
FeCo@Fe@Pd/C	0.5 M KOH + 0.5 M ethylene glycol	-	-	0.272	19
PdRu Nanosponge	0.5 M KOH + 0.5 M ethylene glycol	-	-	0.65	20
PdTe nanowire	0.5 M KOH + 0.5 M ethylene glycol	-	-	0.45	21
RhCu nanobox	1.0 M KOH + 1.0 M ethylene glycol	0.6		0.77 (per mg$_{Rh}$)	22
Glycerol oxidation					
Ni$_{12}$P$_5$ nanoparticles	**1.0 M KOH + 1.0 M glycerol**	**1.65**	**82**	**1.66**	**This work**
Ni$_2$P nanoparticles	**1.0 M KOH + 1.0 M glycerol**	**1.65**	**74**	**1.5**	**This work**
Pd/PEDOT-PSS	0.5 M KOH + 0.5 M glycerol			1.25	23
Pd/HPW/RGO	0.5 M KOH + 0.5 M glycerol	-	-	0.3684	24
PdFePb nanowires	0.5 M KOH + 0.5 M glycerol	-	-	1.45	18
FeCo@Fe@Pd/C	0.5 M KOH + 0.5 M glycerol	-	-	0.26	19
PdAu/P-Se-C	0.1 M KOH + 0.5 M glycerol	-	-	0.58	25
Pd$_3$Ru-NC	0.5 M KOH + 0.5 M glycerol	-	-	0.357	26

* Potentials are converted to RHE scale by following equation:

$$E_{RHE} = E^0_{Ref} + E_{Ref} + 0.059 \times pH$$

Where,

$E^0_{\mathrm{Ag/AgCl}} = +0.197\ V$, considering T= 25 ^{0}C,

$E^0_{SCE} = +0.244$ V, considering T = 25 ^{0}C,

Identification and quantification of products formed after oxidation reaction:

The amount of products was measure quantitatively by NMR. First, a calibration curve was generated for formate, acetate, and acetone by producing aqueous solutions of NaOH (1 M) with known concentrations of formate, acetate and acetone. A volume of 500 µl of each solution with a known concentration was mixed with 100 µl of 0.1 M deuterated solution of TMACl (tetramethyl ammonium chloride) as an internal standard. The final concentration of the products in NMR tube was therefore 5/6 of the known concentration and the TMACl concentration was 16.66 mM. For the calibration of acetone, 500 µl of each known concentration of acetone solution was mixed with 100 µl of 0.1 M aqueous solution of TMACl. D_2O (100 µl) was used for locking the co-axial NMR tube, to avoid the deuterium exchange with acetone protons. The amount of formate, acetate and acetone was quantitively estimated by ^{1}H-NMR spectroscopy (400 MHz).

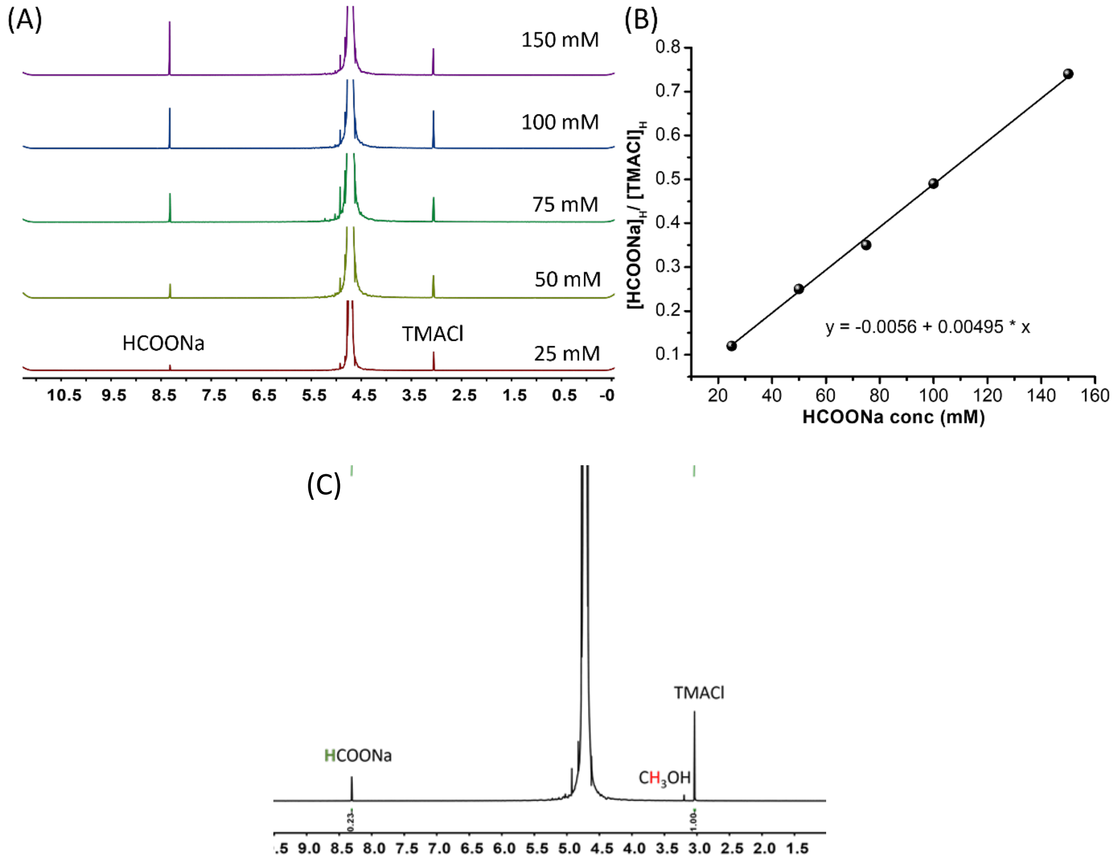

Fig. S19 (A) ^{1}H NMR spectra (400 MHz, locked with D_2O) for the calibration curve of formate. (B) The calibration curve for formate concentration with a linear fit derived from Fig. (A). The Y-axis is proton concentration of $HCOO^-$ normalized with respect to the H concentration of TMACl. (C) ^1H NMR spectra (400 MHz, locked with D_2O) of the analyte solution after completion of chronopotentiometry study for methanol to formic acid conversion. From the calibration curve in (B), it was estimated that 75% of the methanol was converted to formate while 3% methanol was unreacted. The unaccounted 22% of methanol are considered as converted to non-liquid products, such as completely oxidized to yield CO_2.

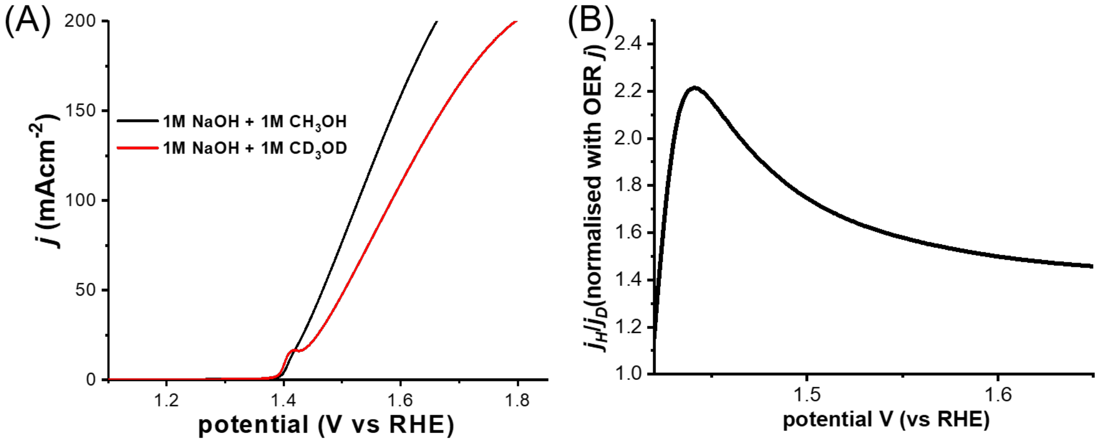

Fig. S20 Comparative experiment to study the kinetic isotope effect using CD_3OD instead of CH_3OH with $Ni_{12}P_5$. (C) A plot of j_H/j_D vs V normalized with respect to OER current density (j_{OER}).

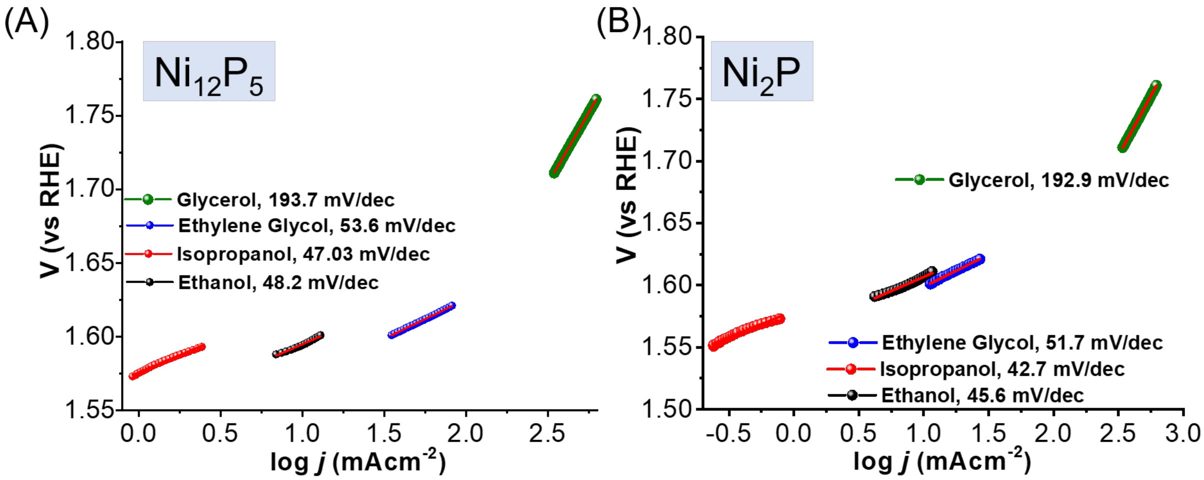

Fig. S21 Tafel slopes for catalysis of ethanol, isopropanol, ethylene glycol and glycerol with (A) $Ni_{12}P_5$ and (B) Ni_2P. Tafel slope derived from **Fig. 4**.

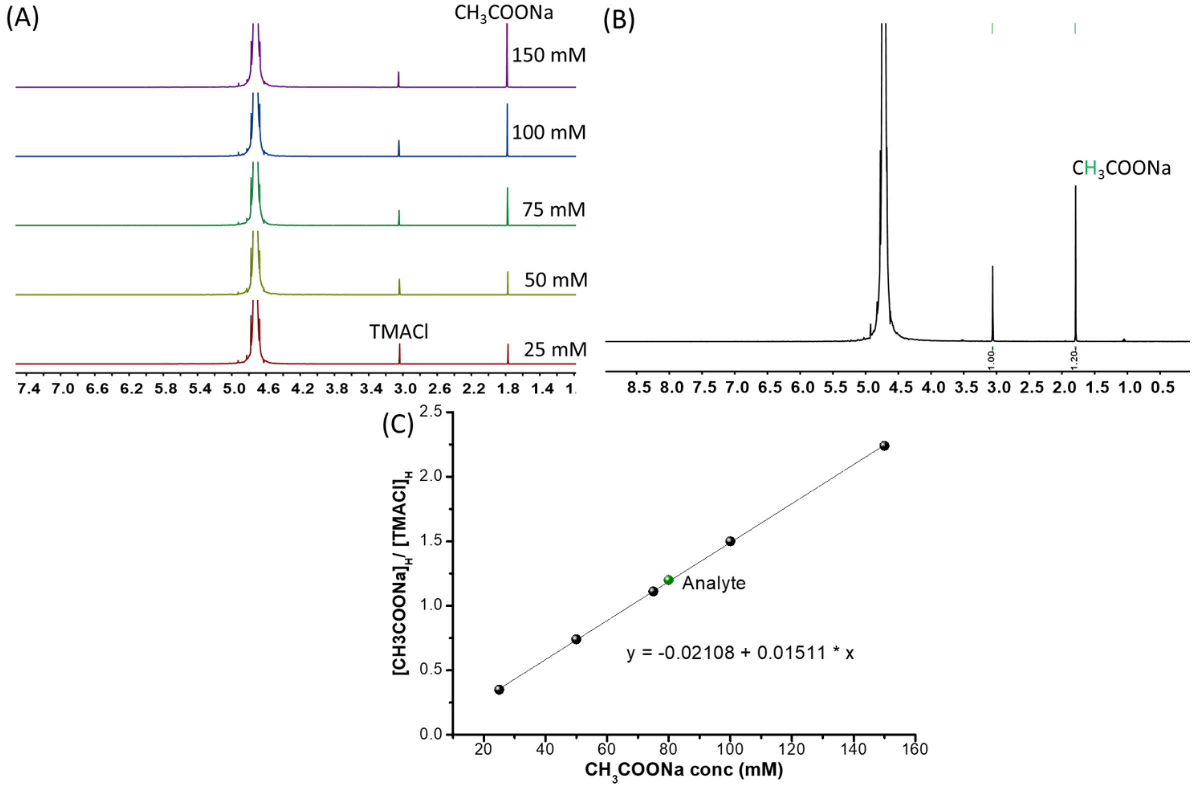

Fig. S22 (A) ^{1}H NMR (400 MHz, D_2O) of different known concentration of acetate ions (acetic acid in 1 N NaOH) in presence of fixed amount of tetramethyl amine chloride (TMACl) (used as internal standard). (C) ^{1}H NMR spectra (400 MHz, locked with D_2O) of the analyte solution after completion of chronopotentiometry study for ethanol to acetic acid conversion.(C) calibration curve with a linear fit derived from Fig. A to detect the amount of acetate formed after conversion (Green dot). The Y-axis is proton concentration of CH_3COO^- normalized with respect to H concentration of TMACl. It was estimated that 98% ethanol was successfully converted to acetate ions and 2% remained unreacted.

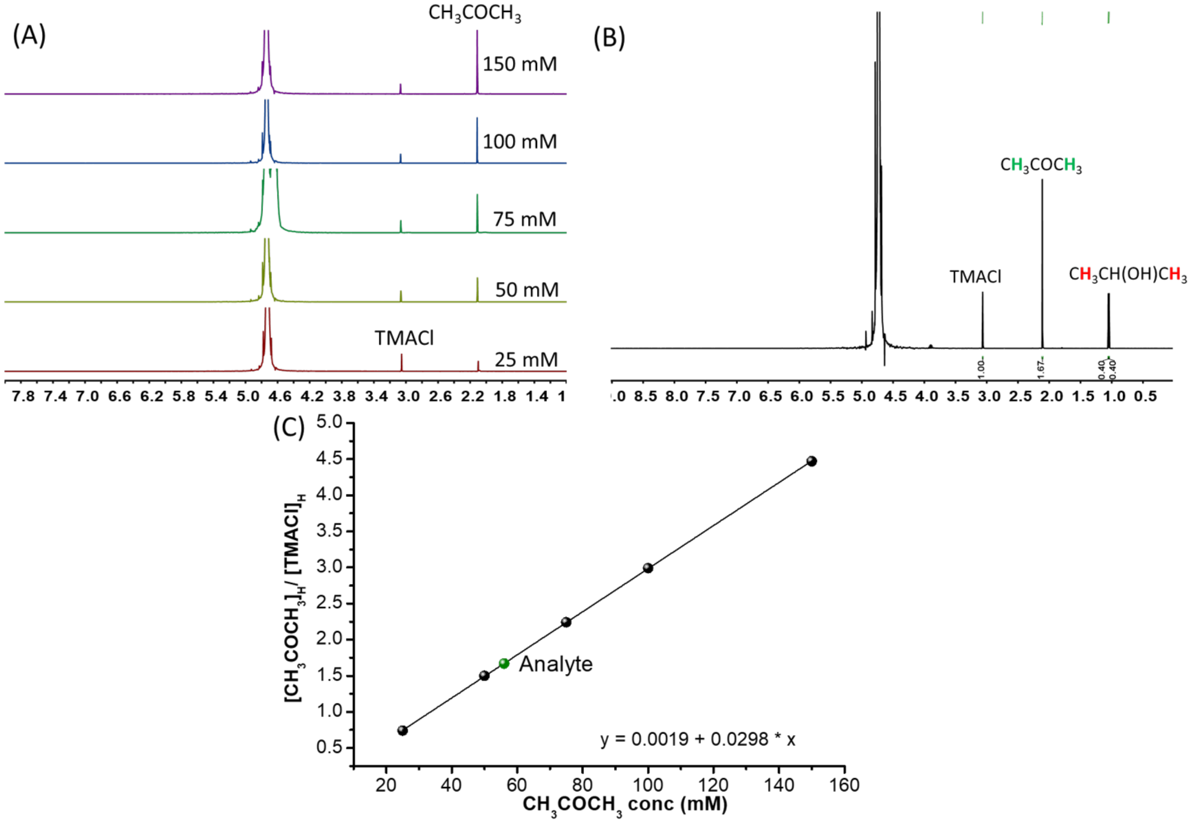

Fig. S23 (A) ^{1}H NMR (400 MHz) of different acetone concentrations in the presence of a fixed amount of tetramethyl amine chloride (TMACl) (used as internal standard). (B) ^{1}H NMR spectra of analyte solution after completion of chronopotentiometry study for isopropanol oxidation to acetone. (C) calibration curve with a linear fit derived from Fig. A to detect the amount of acetone formed after the conversion (Green dot). Y-axis is proton concentration of acetone normalized with respect to H concentration of TMACl. The results show that 67% of the isopropanol was successfully converted to acetone and 33% remained unreacted.

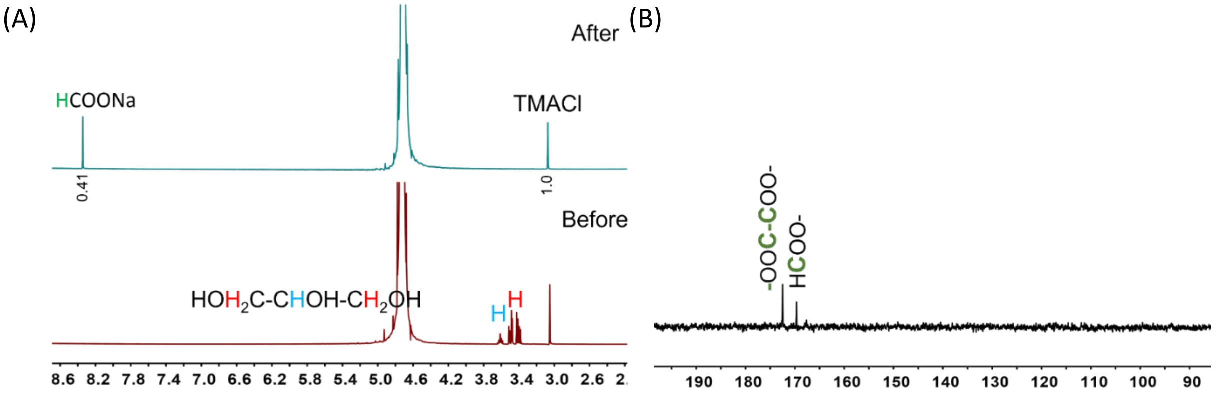

Fig. S24 (A) ^{1}H-NMR spectra of analyte solution containing glycerol before and after chronopotentiometry study. From the calibration curve in **Fig. 19B**, it was estimated that ~ 98 % glycerol is converted to formate ions. No trace of unreacted glycerol was noticed after reaction. (B) ^{13}C-NMR spectra of analyte solution after complete oxidation of glycerol shows the presence of formate and oxalate ions. Each glycerol molecule should produce one equivalent of formate and one equivalent of oxalate. We could detect 98% conversion to formate and a substantial presence of oxalate, although we could not quantify its amount. Preparing a calibration curve for oxalate using C NMR is complicated and beyond the scope of this study, and the ^{13}C-NMR was mainly used to verify the oxalate existence as a marker for the C1-C2 bond cleavage of glycerol.

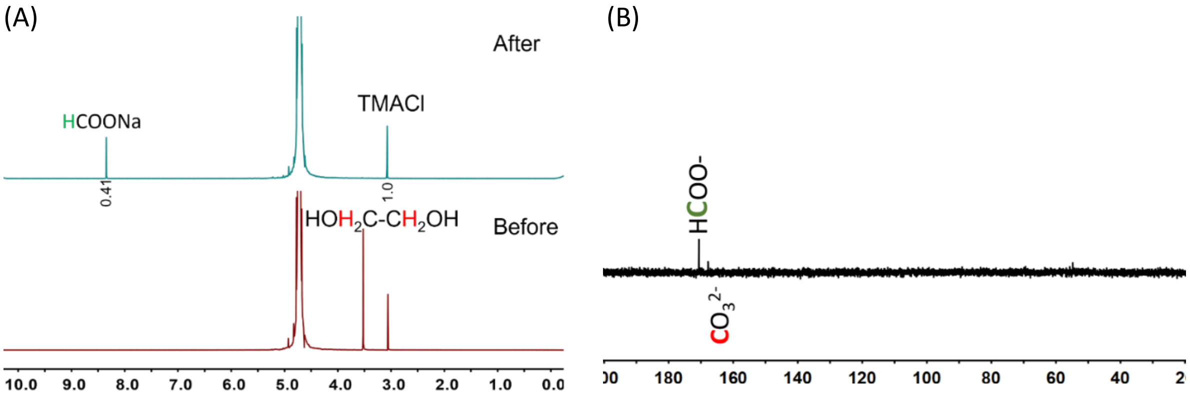

Fig. S25 (A) ^{1}H-NMR spectra of analyte solution containing ethylene glycol before and after chronopotentiometry study. From the calibration curve in **Fig. 19B**, it was estimated that ~ 98 % of ethylene glycol was converted to formate. No trace of unreacted ethylene glycol was noticed after the reaction. (B) ^{13}C-NMR spectra of analyte solution after complete oxidation of ethylene glycol shows the presence of formate and CO_3^{2-} ions. No trace of oxalate was detected which proved the oxidation reaction goes via C-C bond breaking.

References

1. J. Li, R. Wei, X. Wang, Y. Zuo, X. Han, J. Arbiol, J. Llorca, Y. Yang, A. Cabot and C. Cui, *Angew. Chem. Int. Ed.*, 2020, **59**, 20826-20830.
2. C. Liu, W. Zhou, J. Zhang, Z. Chen, S. Liu, Y. Zhang, J. Yang, L. Xu, W. Hu, Y. Chen and Y. Deng, *Adv. Energy Mater.*, 2020, **10**, 2001397.
3. J. Li, Y. Zuo, J. Liu, X. Wang, X. Yu, R. Du, T. Zhang, M. F. Infante-CarriÃ³, P. Tang, J. Arbiol, J. Llorca, Z. Luo and A. Cabot, *J. Mater. Chem. A*, 2019, **7**, 22036-22043.
4. S. L. Candelaria, N. M. Bedford, T. J. Woehl, N. S. Rentz, A. R. Showalter, S. Pylypenko, B. A. Bunker, S. Lee, B. Reinhart, Y. Ren, S. P. Ertem, E. B. Coughlin, N. A. Sather, J. L. Horan, A. M. Herring and L. F. Greenlee, *ACS Catal.*, 2017, **7**, 365-379.
5. J. Li, Z. Luo, Y. Zuo, J. Liu, T. Zhang, P. Tang, J. Arbiol, J. Llorca and A. Cabot, *Appl. Catal. B: Environ*, 2018, **234**, 10-18.
6. Y. Y. Tong, C. D. Gu, J. L. Zhang, H. Tang, Y. Li, X. L. Wang and J. P. Tu, *Electrochim. Acta.*, 2016, **187**, 11-19.
7. Y. Y. Tong, C. D. Gu, J. L. Zhang, M. L. Huang, H. Tang, X. L. Wang and J. P. Tu, *J. Mater. Chem. A*, 2015, **3**, 4669-4678.
8. H. Zhang, C.-D. Gu, M.-L. Huang, X.-L. Wang and J.-P. Tu, *Electrochem. Commun.*, 2013, **35**, 108-111.
9. J. Yang, J. Tan, F. Yang, X. Li, X. Liu and D. Ma, *Electrochem. Commun.*, 2012, **23**, 13-16.
10. X. Cui, P. Xiao, J. Wang, M. Zhou, W. Guo, Y. Yang, Y. He, Z. Wang, Y. Yang, Y. Zhang and Z. Lin, *Angew. Chem. Inter. Ed.*, 2017, **56**, 4488-4493.
11. X. Tong, Y. Qin, X. Guo, O. Moutanabbir, X. Ao, E. Pippel, L. Zhang and M. Knez, *Small*, 2012, **8**, 3390-3395.
12. Q. Luo, M. Peng, X. Sun and A. M. Asiri, *RSC Adv.*, 2015, **5**, 87051-87054.
13. T.-H. Ko, K. Devarayan, M.-K. Seo, H.-Y. Kim and B.-S. Kim, *Sci. Rep.*, 2016, **6**, 20313.
14. Z. Jia, Y. Wang and T. Qi, *RSC Adv.*, 2015, **5**, 83314-83319.
15. N. A. M. Barakat, H. M. Moustafa, M. M. Nassar, M. A. Abdelkareem, M. S. Mahmoud, A. A. Almajid and K. A. Khalil, *Electrochim. Acta.*, 2015, **182**, 143-155.
16. N. A. M. Barakat, M. Motlak, A. A. Elzatahry, K. A. Khalil and E. A. M. Abdelghani, *Inter. J. Hydrogen Energy*, 2014, **39**, 305-316.
17. W. Shi, Q. Wang, F. Qin, J. Yu, M. Jia, H. Gao, Y. Zhang, Y. Zhao and G. Li, *Electrochim. Acta.*, 2017, **232**, 332-338.
18. R.-L. Zhang, J.-J. Feng, L. Zhang, C.-G. Shi and A.-J. Wang, *J. Colloid Interface Sci.*, 2019, **555**, 276-283.
19. O. O. Fashedemi and K. I. Ozoemena, *Electrochim. Acta.*, 2014, **128**, 279-286.
20. P. Bi, W. Hong, C. Shang, J. Wang and E. Wang, *RSC Adv.*, 2016, **6**, 12486-12490.
21. W. Hong, J. Wang and E. Wang, *CrystEngComm*, 2015, **17**, 9011-9015.
22. B. Qiao, T. Yang, S. Shi, N. Jia, Y. Chen, X. Chen, Z. An and P. Chen, *Small*, 2021, **17**, 2006534.
23. A. Nakova, M. Ilieva, T. Boijadjieva-Scherzer and V. Tsakova, *Electrochim. Acta.*, 2019, **306**, 643-650.
24. J. Hu, X. Wu, Q. Zhang, M. Gao, H. Qiu, K. Huang, S. Feng, Y. Yang, Z. Liu and B. Zhao, *Electrochem. Commun.*, 2017, **83**, 56-60.
25. Y. Dong, W. Wang, Y. Wang, P. Wang, L. Zhang and Z. Lei, *J. Taiwan Inst. Chem. Eng.*, 2018, **93**, 500-508.
26. B. Ran, S. Liu, J. Zhao, T. Tan, B. Liang and W. Wang, *J. Mater. Sci.*, 2018, **54**, 4579-4588.